Low-cost wavefront sensing using artificial intelligence (AI) with synthetic data

Baudat, Gaston

Gaston Baudat, "Low-cost wavefront sensing using artificial intelligence (AI) with synthetic data," Proc. SPIE 11354, Optical Sensing and Detection VI, 113541G (1 April 2020); doi: 10.1117/12.2564070

SPIE.

Event: SPIE Photonics Europe, 2020, Online Only, France

Low-cost wavefront sensing using artificial intelligence (AI) with synthetic data

Gaston Baudat
Innovations Foresight, LLC, Glenmoore, PA, USA 19343

ABSTRACT

We present a low-cost stand-alone AI based wavefront sensor (AIWFS) trained only with synthetic data. A simple defocused image of a source provides non-ambiguous phase retrieval competing with traditional wavefront sensors such a Shack-Hartmann (SH) sensor. An artificial neural network (ANN) is trained to output the Zernike coefficients, or any other relevant figures of merit, exclusively from synthetic data. The synthetic data typically contains random Zernike coefficients or wavefront, noise, as well as a defocus error to avoid any stringent accuracy requirement. Once trained, the AIWFS can be used directly on many other applications without any retraining. In its simplest form, the AIFWS's hardware is just a camera taking defocused images of a point source, like a star. However, with the proper synthetic data, many types of source and optical layouts can be accommodated, such multi-point, or extended, sources to simultaneously determine both on-axis and field-dependent wavefront performance, from a single measurement. In applications using actual stars, the NN also provides the Fried's parameter as an estimation of atmospheric turbulence. The ANN outputs are computed directly there is no numerical iteration nor any convergence consideration. The system can run at video rates, in real time, and therefore is suitable for analyzing systems with vibrations or moving parts. The AIWFS only requires a single camera making it a simple cost-effective solution that can take advantage of an existing camera that may already be in an optical system. This paper shows results using AIFWS for telescopes with both actual and artificial stars.

Keywords: Artificial intelligence, machine learning, wavefront sensing, field-dependent wavefront sensing, multi-source wavefront sensing, extended source wavefront sensing, low cost fast wavefront sensing.

1. INTRODUCTION

Wavefront sensing is important for quantitative evaluation of optical systems. Applications are many, such as metrology, optical alignment, adaptive optics (AO), astronomy, ophthalmic, etc. Common wavefront sensors include Shack-Hartmann (SH) wavefront sensor and curvature sensing wavefront sensor. A SH wavefront sensor requires a lenslet array which is, often expensive, and which requires accurate alignment. Furthermore, its dynamic range is limited by adjacent sub-pupil image overlaps. A curvature sensing wavefront sensor uses several carefully taken defocused images of a point source. Curvature sensing is based on the irradiance transport equation solved with iterative numerical techniques. Hickson and Burley[1] have shown that, under some conditions, a single defocused image contains enough information to uniquely determine the phase of an incident wavefront. The minimum defocus required is function of the amplitude of higher order aberrations. Nishizaki[2] et al. proposed using AI for learning the Zernike coefficients from a single measured defocused image. Their ANN is a deep convolution neural network (CNN) trained from, and associated with, a physical system using a spatial light modulator (SLM) for emulating Earth atmospheric induced turbulence wavefront errors in the context of AO for astronomy. Therefore, this approach requires a new learning dataset and training phase for different optical systems and related parameters. Since actual data is required, applications of this strategy is limited to those systems for which one can physically emulate and control wavefront errors using a SLM or equivalent methods. This paper presents a low-cost, stand-alone AI based wavefront sensor designed to be as generic as possible, so that it is independent of a given physical system or actual data. An ANN is trained to output the Zernike coefficients, or any other relevant figures of merit, such as the wavefront itself, exclusively from synthetic data. The simulated synthetic defocused images are normalized in relation with the class of optical systems to be analyzed such the ANN output values are as universal as possible. A pre-processing and conditioning step is responsible for matching the synthetic data with the optical parameters such as focal length, wavelength, aperture, as well as the physical camera resolution and performances used to provide actual values. The synthetic data typically includes noise, as well as some defocus error to avoid any stringent accuracy requirement on camera position.

Optical Sensing and Detection VI, edited by Francis Berghmans, Anna G. Mignani, Proc. of SPIE
Vol. 11354, 113541G · © 2020 SPIE · CCC code: 0277-786X/20/$21 · doi: 10.1117/12.2564070

Once trained, the AIWFS can be used directly on many other applications without retraining the ANN. In its simplest form, the AIFWS's hardware is just a camera taking defocused images of a single point source. However, with the proper synthetic data, many types of source and optical layouts can be considered, such multi-point sources for on and off axis wavefront sensing at once, or extended sources. The AIWFS is a cost-effective solution, which can take advantage of a camera already in the system. The ANN outputs are computed directly and unlike in curvature sensing, there is no need for numerical iteration, which, eliminates convergence considerations. This paper shows results using AIFWS for telescopes with either an actual or an artificial star as a point source.

2. METHODOLOGY

2.1 Background and concept

The relative intensity fluctuation in a defocused image of a telescope is function of the wavefront curvature as shown by Roddier and Roddier[3] in the context of curvature sensing and discussed by Hickson[1] when using a single defocused star, the relative intensity variation is given by:

$$\frac{\Delta I}{I_0} = -\frac{fl\lambda}{2\pi(f-l)}\left[\nabla^2\phi(\vec{\mathrm{r}}) - \delta(r-R)\frac{\partial\phi(\vec{r})}{\partial r}\right] \quad (1)$$

Where ϕ is the wavefront phase, λ the wavelength under consideration, f and R are respectively the focal length and the aperture radius of the telescope. l is the distance from the exit pupil to the defocused image plane, while $\vec{r}$ is the incoming ray position vector in the pupil and r its length. I_0 is some reference intensity signal, such as the average value of the defocused image intensity or similar, or some constant related to a given optical system, source and defocus. Equation (1) is derived from the irradiance transfer equation for which $\nabla^2\phi(\vec{\mathrm{r}})$ is the divergence of the gradient, or Laplacian. It describes the local curvature of the wavefront and $\delta(r-R)$ a linear impulse distribution around the edge of the pupil. ΔI is the intensity fluctuation and from equation (1) one sees that its relative variation, in a single defocused image, is related to the wavefront curvature. Therefore, one can extract the wavefront phase from the relative intensity $\Delta I/I_0$. Equation (1) is a first order approximation valid when $fl/(f-l)$ is small, which is true for highly defocused images. There is no general analytic solution of the differential equation (1). In practical applications, iterative numerical methods are used for extracting the wavefront from the defocused image intensity. Those typically use gradient descent methods or other optimization techniques however, they require an iterative solution and may face local minima and other related convergence issues, especially if the aberrations are large. Tokovinin and Heathcode[4] proposed an interesting approach to overcome those limitations. They seed an optimization algorithm based on the first moments of the defocused image intensity. Still an iterative model fitting procedure is necessary to solve for the wavefront, which may be time consuming and by nature of this non-linear problem, prone to local minima as well. With our approach we learn from simulated samples the inverse-model relating the relative intensity fluctuations of a defocused image to its wavefront using an ANN and synthetic data.

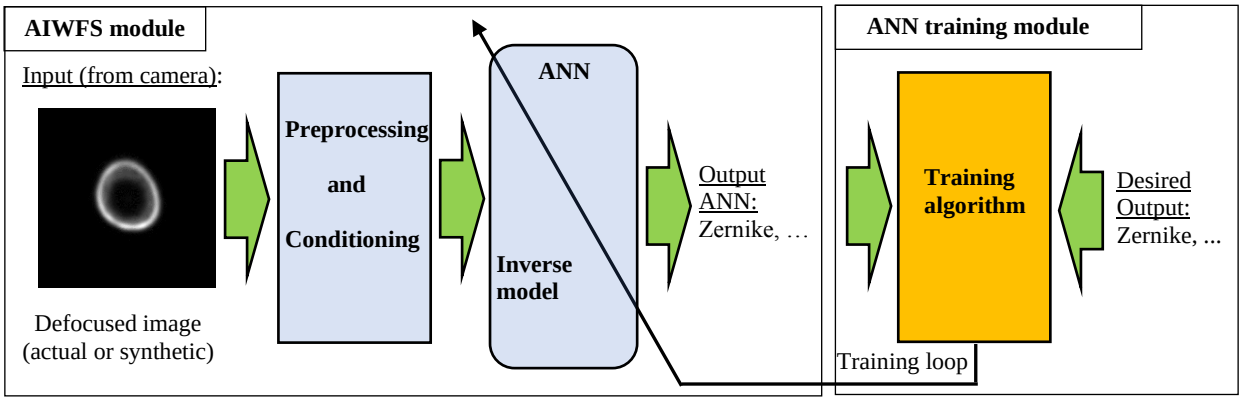

Figure 1. AIWFS block diagram, concept and training procedure

This method, outlined in figure 1, has the advantage that the optimization task is done only once, beforehand, and when a suitable inverse model has been learned with enough accuracy and generalization performance, it can be used in real time without any consideration of convergence, iteration time, or local minima concerns. A key goal has been to make this method as generic as possible, independent of actual data from a physical optical system (such as a telescope) to make it applicable for a large class of system with the same inverse-model, using the same ANN training. Although this is not a limitation of the method, in this paper, we have chosen to apply it to telescope optical alignment (known as collimation) in the context of astronomical applications with either an actual star or an artificial star (in double pass). Figure 2 shows the basic setting, with ΔZ the defocus distance from the focal plane to the sensor plane where the defocused image is formed.

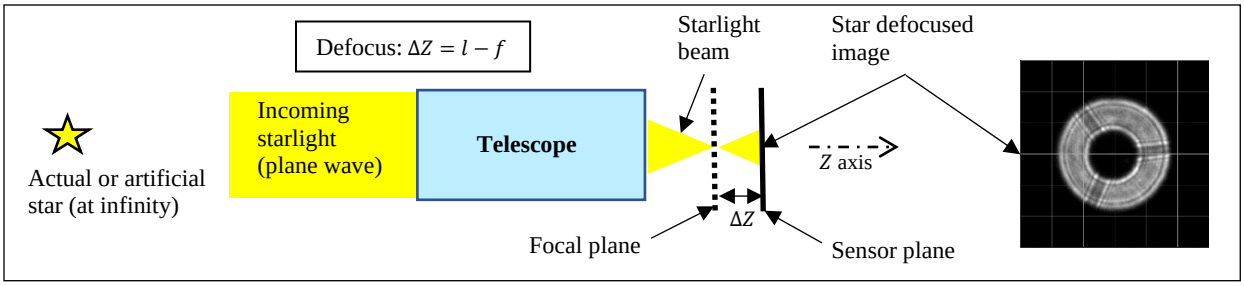

Figure 2. AIWFS in the context of a telescope and a star at infinity.

2.2 Data preprocessing and signal conditioning

The synthetic data is computed, for a given telescope class, using the scalar diffraction theory and the FFT for modeling the defocused image. A class of telescope is defined by its central obstruction $0 < \varepsilon \leq 1$, expressed in percent of the telescope aperture diameter D obscured by a centered circular secondary mirror. Although one can train an ANN for a large range of ε values, which would become an input data for the ANN, we found that it is easier to do this using a limited range of central obstruction. In this paper, we have only considered circular apertures (axially symmetric systems), the most common situation, but other shapes could be easily handled. In this context, we have chosen to use the Zernike radial annular polynomials for expressing the wavefront phase errors (aberrations) across the telescope pupil as well as, when applicable, the Fried[5] parameter, or coherence length, r_0 for the strength of the Earth atmospheric turbulences, also known as seeing. Various levels of noise are added to the synthetic data to account for sensor, electronic and shoot noise, as well as scintillation. In order to be as generic as possible, simulations are carried out using a normalized optical telescope for synthetic data generation and datasets used in ANN training, validation and generalization tests. The normalized telescope assumes the following values (units in meter otherwise specified in this paper):

$$R = 1m \text{ and } \lambda = 1m \tag{2}$$

Where $R = D/2$. For the simulation the pupil is typically uniformly sampled with $M = 100$ points across its radius (including the central obstruction, if any), or a little more than thirty thousand samples covering the entire telescope aperture. By chosen a $NxN = 1024x1024$ points FFT this leads to about 12 samples across of the first zero central region of the diffraction limited PSF of a star (Airy disk). The FFT is padded with zeros for the samples outside the pupil or inside the central obstruction. Although ones could use a rectangular FFT, the axially symmetric nature of the problem calls for a squared one, hence squared related defocused images, which is what is used in this paper, but this is of course not a limitation of this approach. By using the values from (2), assuming a monochromatic light source in an axially symmetric context, the related normalized simulation angular resolution θ_s of the diffraction pattern for the synthetic data is given, in radian, by:

$$\theta_s = \frac{M}{N} \tag{3}$$

Which for the sampling strategy chosen leads to an effective synthetic data normalized angular resolution θ_{se} of:

$$\theta_{se} = \frac{100}{1024} \cong 0.0977 \text{ radians} \tag{4}$$

On the other hand, with the same sampling, the associated actual diffraction simulation angular resolution θ_a of a physical telescope of aperture $D = 2R$ and for a wavelength λ is given by:

$$\theta_a = \theta_s \frac{\lambda}{R} \tag{5}$$

The size px_a of the resulting simulated pixels for the actual telescope at the focal plane, using (5) and assuming $R \gg \lambda$ and $f \gg \Delta z$, is given by:

$$px_a = \theta_s \frac{\lambda}{R} f = \theta_s \lambda 2\, f/\# \tag{6}$$

Where $f/\#$ is the f-number of the telescope. As an example, for a $f/12.5$ telescope at 520nm with $N = 1024, M = 100$, the actual simulated pixel size at the focal plane is:

$$px_a = \frac{100 \cdot 520 \cdot 10^{-9}}{1024} 2 \cdot 12.5 = 1.27 \mu m \tag{7}$$

In comparison, the first zero diameter of the Airy disk of such telescope is $2.44 \cdot 520 \cdot 10^{-9} \cdot 12.5 = 15.86\ \mu m$ which represents about 12 pixels of $1.27\ \mu m$. We observed that sampling rate leads to a good enough resolution for practical applications, especially with defocused images. Also, the resulting size of the simulated pixel for actual telescopes is usually smaller than the most common camera sensor pixel size for usual $f/\#$ values. The ANN is fed with images having a fix resolution of LxL samples, typical values are $L = 128$ and $L = 256$. Therefore, the raw synthetic data needs to match the NN input size and since usually $M > L$ we use a decimation process to resize the image. A similar process is applied when the AIWFS, after a successful training of the ANN on the normalized synthetic data, is used on actual defocused images for a given camera and telescope. Based to px_a, L, M and the size of the actual camera pixel px_c one computes the ratio K for matching the camera image with the ANN input.

$$K = \frac{px_a}{px_c} \frac{M}{L} \tag{8}$$

If $K > 1$ the camera pixel size is smaller than the ANN pixel size $px_a L^{-1} M$ for the physical setup and the image is decimated by a factor K for matching the ANN input pixel size. If $K < 1$ then the image is interpolated instead. As an example, for a $f/12.5$ telescope, $L = 256$ and a camera pixel size $px_c = 3.8 \mu m$, using (7) and (8), leads to:

$$K = \frac{1.27 \cdot 10^{-9} 1024}{3.8 \cdot 10^{-9} 256} = 1.337 \tag{9}$$

Therefore, the camera image needs to be resized down by about 30% to match the ANN input pixel size for this telescope, camera, ANN and synthetic data used for the training. The camera defocused image is preprocessed to take care of any offset, fix pattern noise, hot pixels and other artifacts. For instance, this can be done by the subtraction of a dark frame taken under the same conditions, or any suitable means. Noise filtering and other processing may be applied as well. Since usually the camera frame is significantly larger than the defocused image of interest, the last step is the extraction of the defocused image from the camera image. This is a straightforward operation, first one locates the center of the defocused image using a centroid algorithm, or similar a method, then one crops the camera resized image to the size LxL.

2.3 Training of the ANN

For training the ANN one generates normalized defocused images (SD) across ranges of the Zernike coefficients and r_0 values, if applicable. Alternate approaches are of course possible, such directly sampling an aberrated wavefront. In this case, the ANN outputs would be the sampled wavefront itself instead of the Zernike coefficients or other aberration terms. In this paper, we preferred a parametric approach which describes the wavefront error through the Zernike radial annular polynomials. Although this is not a limitation of the method, here we have used the AIWFS for telescope collimation and therefore we are mainly interested in the lower 3rd order aberrations, since the optical surface figures are assumed to be near perfection. Monitoring the low order aberrations is enough for this task, but higher order aberrations can certainly be considered with the AIWFS. Table 1 shows the Zernike radial annular polynomial considered in our experiments.

Table 1. Orthonormal Zernike radial annular polynomials used for synthetic data and ANN training in this paper.

Name	OSA index	Standard OSLO index	Polynomial $\int_0^{2\pi}\int_0^1 Z_j^2 dr d\theta = \pi \qquad \int_0^{2\pi}\int_0^1 Z_i Z_j dr d\theta = 0 \ \forall i \neq j$ $0 < r \leq 1 \qquad 0 < \epsilon \leq 1 \qquad 0 \leq \theta \leq 2\pi$
Defocus	Z_4	Z_3	$\sqrt{3}(2r^2 - 1 - \varepsilon^2)/(1 - \varepsilon^2)$
Vertical astigmatism	Z_5	Z_4	$\sqrt{6}\left(r^2/\sqrt{1+\epsilon^2+\epsilon^4}\right)cos(2\theta)$
Oblique astigmatism	Z_3	Z_5	$\sqrt{6}\left(r^2/\sqrt{1+\epsilon^2+\epsilon^4}\right)sin(2\theta)$
Horizontal coma	Z_8	Z_6	$\sqrt{8}\,[3r^3(1+\epsilon^2) - 2r(1+\epsilon^2+\epsilon^4)]/\left[(1-\epsilon^2)\sqrt{(1+\epsilon^2)(1+4\epsilon^2+\epsilon^4)}\right]cos(\theta)$
Vertical coma	Z_7	Z_7	$\sqrt{8}\,[3r^3(1+\epsilon^2) - 2r(1+\epsilon^2+\epsilon^4)]/\left[(1-\epsilon^2)\sqrt{(1+\epsilon^2)(1+4\epsilon^2+\epsilon^4)}\right]sin(\theta)$
Primary spherical	Z_{12}	Z_8	$\sqrt{5}(6r^4 - 6r^2(1+\epsilon^2) + 1 + 4\epsilon^2 + \epsilon^4)/(1-\epsilon^2)^2$
Oblique trefoil	Z_9	Z_9	$\sqrt{8}\left[r^3/\sqrt{1+\epsilon^2+\epsilon^4+\epsilon^6}\right]cos(3\theta)$
Vertical trefoil	Z_6	Z_{10}	$\sqrt{8}\left[r^3/\sqrt{1+\epsilon^2+\epsilon^4+\epsilon^6}\right]sin(3\theta)$
Secondary spherical	Z_{15}	Z_{24}	$\sqrt{7}(20r^6 - 30r^4(1+\epsilon^2) + 12r^2(1+3\epsilon^2+\epsilon^4) + 1 + 9\epsilon^2 + 9\epsilon^4 + \epsilon^6)/(1-\epsilon^2)^3$

In order to detect possible stress on the mounted optics we have added the trefoil and the secondary (5^{th} order) spherical aberrations. In this paper, we use the OSA index for the Zernike coefficients. There are 3 datasets for the ANN training phase. The first is the learning dataset, which is used for optimizing the ANN itself (synaptic weights) and this dataset is the largest, typically between 300,000 to 500,000 samples, or more. The second is the validation dataset which is used to monitor the generalization performance of the ANN during the training procedure in order to stop it before overlearning, this dataset size is between 10,000 to 50,000 samples. The third is the test dataset used after training to estimate the inverse model generalization capability, performance and accuracy. All the datasets are generated from the same independently identically distributed uniform random variable simulations across the range of Zernike coefficients and r_0 values, when under seeing limited conditions.

3. EXPERIMENTS

Several experiments have been carried out on an optical bench in the lab in double pass with a pellicle beam splitter and a pinhole in the telescope focal plane acting as an artificial star (see figure 6), and on the sky using real stars under seeing limited conditions.

3.1 Comparison with a Shack Hartmann wavefront sensor on an optical bench

We compare the AIWFS approach on a 90mm aperture f/13.9 Maksutov-Cassegrain telescope with a 32% ($\varepsilon = 0.32$) central obstruction against a Shack-Hartmann analyzer using a 40x40 lenslet array on an optical bench in double pass. The source is made of a 5µm pinhole illuminated by a white LED and located at the scope focal plane acting as an artificial star. A pellicle beam splitter is used to avoid any sphero-chromatic aberrations. The autocollimator return flat is made of ZERODUR® with 100mm diameter, 20mm thickness, and a flatness specification of 0.010 wave from 400nm to 2000nm. Figure 6 shows the setup for a 24mm, $f/12.5$ refracting telescope in similar double pass configuration. The ANN inverse model was trained with 300,000 simulated defocused images of 128x128 pixels. Nine Zernike radial annular coefficients are considered, Z_3 to Z_9, as well as Z_{12} and Z_{15}, see the table 1 for index reference. The defocus Z_4 coefficient is not reported in the results. The SH wavefront sensor specified accuracy is 0.02 wave (20mw) rms, the estimated AIWFS accuracy, over 30,000 test samples, is at 0.03wave (30mw) rms for this simulation and associated ANN. Using larger L values leads to a significant higher accuracy, in the range of 4mw, as seen in section 3.3.

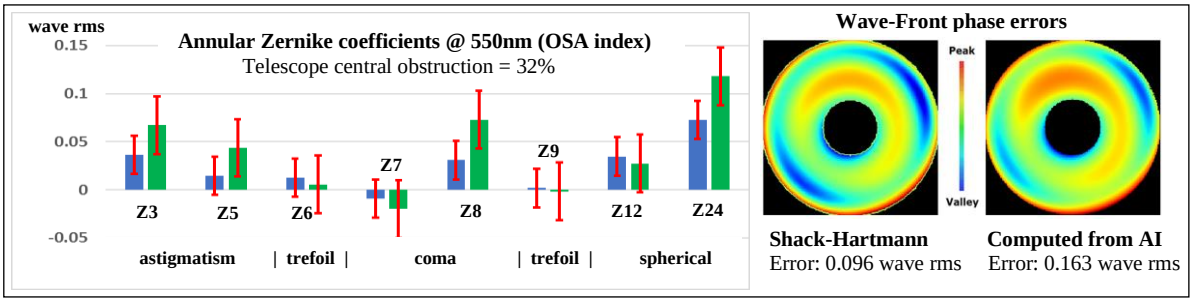

Figure 3. Maksutov-Cassegrain telescope: SH (blue) v.s. AI wavefront sensor (green) analysis on an optical bench in double pass with an artificial star and a white LED. The red error bars are one standard deviation

The figures 3 shows the rms wavefront deviation along with the Zernike coefficients for both, the Shack Hartman results shown in blue and the AIWFS shown in green, as well as the associated 1 sigma error bars (in red,). The reconstructed wavefront 2D error plots are also provided for qualitative evaluation. Since the SH analyzer measures higher order aberrations, more than 20 Zernike polynomials are used, so we may expect some differences between both methods. Still the AIWFS rms values track closely the SH wavefront sensor results. Zernike coefficients, for both systems, were computed at 550nm near the middle of the white LED bandwidth. One can see that even though the AIWFS was trained with a monochromatic light source, it provides good polychromatic results. It should be noted that we could simulate polychromatic synthetic data for training the ANN with our approach too.

3.2 Wavefront analysis using an actual star under seeing limited conditions

Telescope wavefront analysis on a bench, in double pass, with an artificial star may not be always practical or feasible, especially for large apertures. High quality flat mirrors are expensive, and the telescope needs to be moved to some lab for testing which takes time and some effort limiting the frequency at which such test can be performed. Therefore, there is a need for onsite fast wavefront analysis using actual stars. The AIWFS technology provides a unique opportunity for accomplishing this goal without any extra hardware using, in most cases, the installed imaging camera and focusing mechanism. In this context one can perform real time optical alignment (collimation) and collect data as often as one may need for predictive maintenance and quality assessment of the telescope from nights to nights, or over the course a given night. This could be also very appealing for remote and aerospace applications, such as space telescopes or probes, for which there is no easy access to the system, while extra hardware for wavefront analysis and monitoring the optics, for performing any corrective actions, is not possible or limited by space and weight requirements. When using an actual star on Earth one must account for the seeing which blurs the stellar images. The Kolmogorov's turbulence theory and numerical simulations provide a relation between the Fried's parameter r_0 and the FWHM in radian, known as β, of the seeing limited PSF of a star.

$$\beta \cong 0.98\frac{\lambda}{r_0} \tag{9}$$

The blurred stellar profile is often expressed using a Moffat[6] function, however from a practical standpoint a Gaussian function gives good results, especially for defocused star images. In our experiments, under seeing limited conditions, one exposes a defocused star for several minutes in order to average out the seeing such the resulting image can be understood as a Gaussian kernel acting as a low pass filter convoluted with the seeing free defocused image. Using (9) the seeing induced kernel standard deviation σ, in radian, is given by:

$$\sigma = \frac{\beta}{2\sqrt{2\ln(2)}} \cong 0.4162\frac{\lambda}{r_0} \tag{10}$$

The relation (10) is used for the synthetic data simulations under seeing limited conditions in this paper. The figure 4 shows a 256mm aperture @ $f/8$ Ritchey-Chretien telescope AIWFS analysis, on the sky, using an actual star under astronomical seeing limited conditions (Fried's parameter $r_0 \cong 49mm$). The ANN uses resized cropped frames from an imaging camera having $5.4\mu m$ pixel size for a total 16,384 pixels ($L = 128$). It was trained to output the annular Zernike coefficients (the same than in section 3.1) as well as the seeing strength for: $35mm \leq r_0 \leq 85mm$ from 200,000 simulated samples. Scintillation was also simulated.

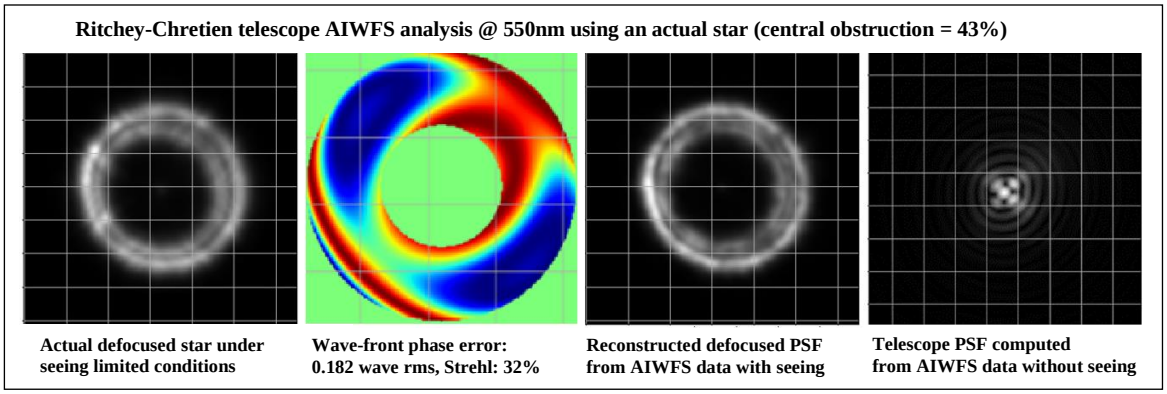

Figure 4. Ritchey-Chretien telescope AIWFS analysis on the sky under astronomical seeing limited conditions.

The data indicates that this telescope mirrors required alignment. The third image from the left on figure 4 is the reconstructed defocused PSF simulated using the Zernike coefficients from the AIWFS as well as the Fried's parameter r_0, scintillation (intensity fluctuations) has been added too. Although this is a random realization of the seeing, it is realistic and quite close to the actual defocus star image (first on the left). One difference being the secondary mirror spider diffraction patterns visible on the actual image. Those have not been simulated here, but they do not seem to have any appreciable impact on the wavefront analysis and related Zernike coefficients. The right image of figure 4 shows the telescope PSF computed from the Zernike coefficients, without any seeing and defocus. It is the PSF one would see using such scope from space. It exhibits a large level of astigmatism as well as some spherical aberration due to misalignment of the two telescope mirrors.

3.3 Real time field dependent wavefront analysis

The AIWFS is flexible by nature and it can be applied to different type of sources, as long as, one can compute the related synthetic data for the training. Since the camera usually sees a much larger FOV than a single defocused image of a point source on can recover, at once and in real time, on and off axis data in the context of field dependent wavefront analysis. There are many benefits, among them: There is no need for any extra off axis wavefront sensors nor any parts in motion for scanning the field with a single sensor. A large FOV is therefore accessible from one single image with the same hardware providing fast field aberration data acquisition capability. Using a 24mm diameter $f/12.5$ achromatic refracting telescope, in double pass, we show field dependent data coming from a line of 7 pinholes, $10\mu m$ each with a 1.5mm pitch. The related optical bench is shown on figure 6. The pinholes are illuminated with a white LED. A green filter in front for the camera with a central wavelength at 520nm and a FWHM of 65nm is used to narrow the bandwidth of the light source.

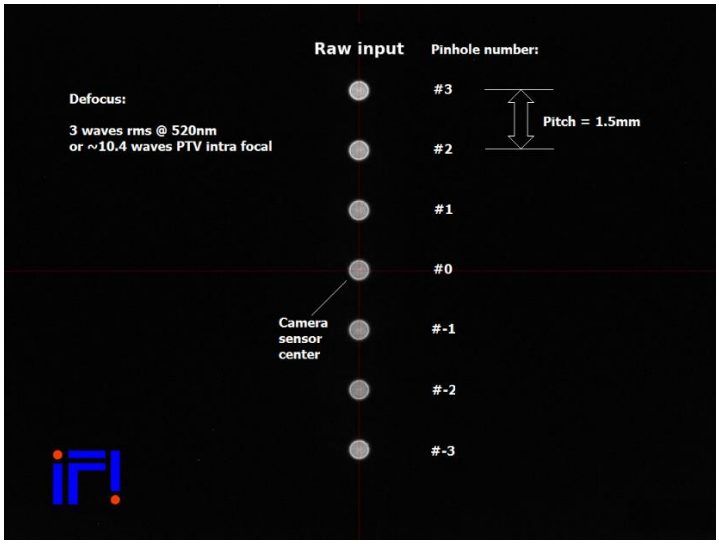

Figure 5. Defocused image of a 7 pinholes line for field dependent wavefront analysis. The pinhole pattern pitch is 1.5mm. The pinhole #0 is at the center of the camera sensor, on axis.

The refracting telescope is made of a single fully AR coated achromat with a 300mm focal length. The flat mirror has a flatness of, or better than, 10^{th} wave. In figure 5, one sees the raw defocused image of the pinholes. The pinhole #0 is imaged, on axis, at the center of the camera sensor. The red lines indicated the horizontal and vertical axes. The two extreme pinholes #-3 and #3 are, at respectively, -4.5mm and +4.5mm off axis on the vertical direction, which corresponds to +/-0.86 degrees of field.

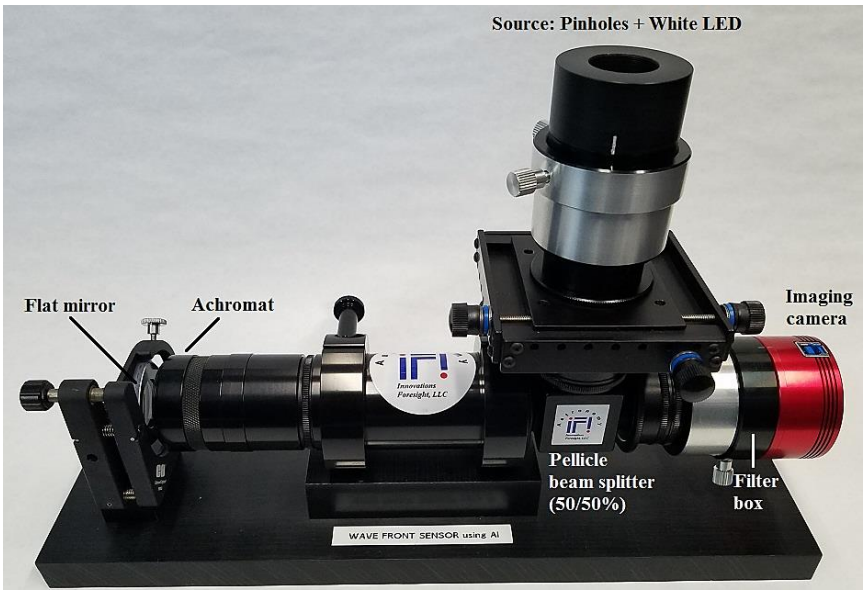

Figure 6. Optical bench: 24mm diameter $f/12.5$ achromatic refracting telescope in double pass configuration

The monochrome camera features a 16 M-pixel sensor with a 21.9mm diagonal and squared pixels of $5.4\mu m$. Data acquisition is done with a 12 bits resolution. The camera can transmit data up to 14.7 frame per second. The ANN is fed with 256x256 pixels ($L = 256$) resized frames and was trained with 500,000 simulated samples at 520nm to deliver high wavefront analysis accuracy. The synthetic data was computed without any seeing and central obstruction ($\varepsilon = 0$). From the validation data one estimated an AIWFS accuracy of 0.004 wave (4mw) rms. Using the achromat model, we compared, after removing the flat mirror astigmatic contribution, on table 2 the theoretical monochromatic Zernike aberrations computed using OSLO and the AIWFS values for the two most off axis pinholes, #+3 and #-3. Considering the polychromatic nature of the measurement, the tolerances of the lens surfaces and mechanical alignment errors the AIWFS captured, within few 10mw, the off axis astigmatism and the primary spherical aberrations quite well.

Table 2. AIWFS field aberrations versus the achromat model (OSLO). Flat mirror astigmatism removed

Aberrations [wave]	**Achromat model (OSLO) Off axis: +/-4.5mm**	**AIWFS Off axis: -4.5mm**	**AIWFS Off axis: +4.5mm**
Vertical astigmatism	0.092	0.061	0.081
Oblique astigmatism	0	0.014	0.005
Horizontal coma	-0.002	-0.013	-0.010
Vertical coma	0	0.003	-0.013
Primary spherical	-0.025	-0.018	-0.018
Oblique trefoil	0	0.001	0.002
Vertical trefoil	0	-0.006	0
Secondary spherical	0	0.009	0.009

Figure 7 top wavefront error color plots show, from left to right, the extreme off axis pinhole #-3 at -4.5mm, the on axis pinhole #0 and the extreme off axis pinhole #3 at +4.5mm. The Strehl ratios (SR), rms and PTV wavefront errors are also provided. An on axis astigmatism of 14mw can be traced back to the flat mirror in front of the telescope. This astigmatism has an orientation consistent with the location of the mirror mount contact points. The on axis wavefront error with the mirror astigmatism removed is shown in figure 8.

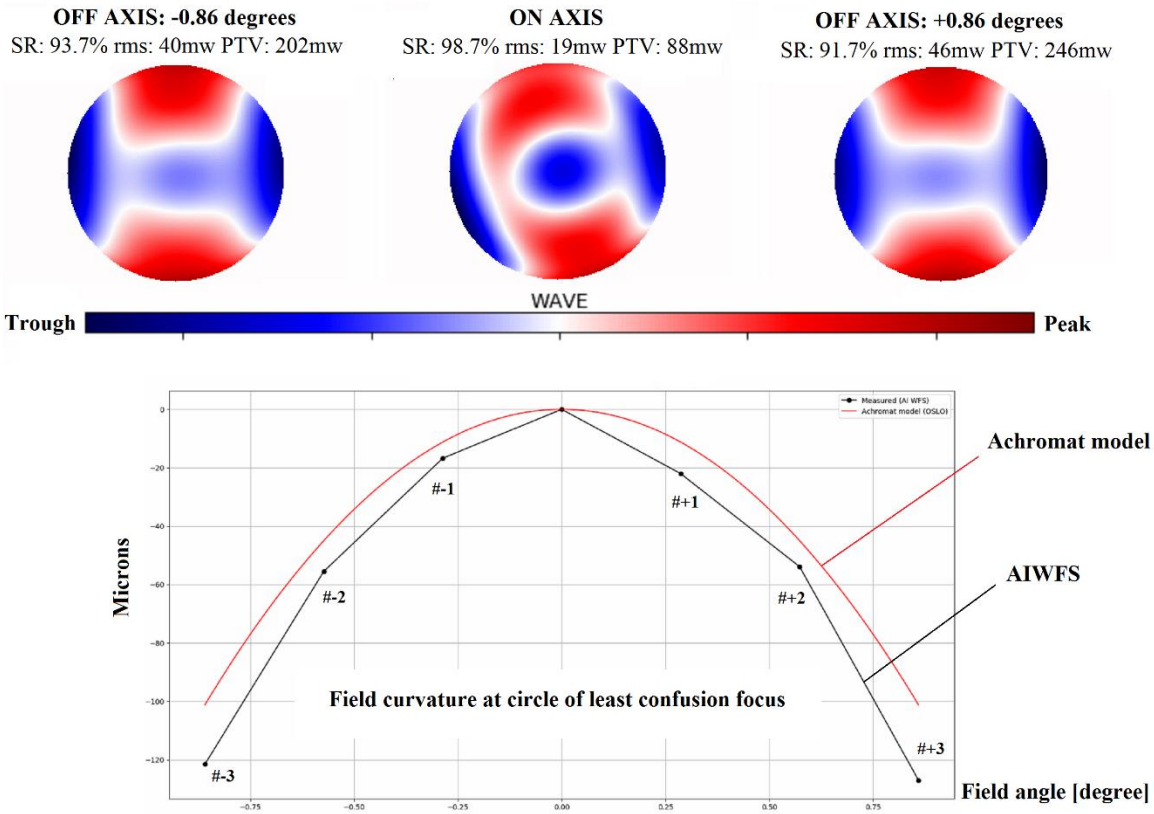

Figure 7. Optical bench refracting telescope field dependent wavefront analysis. Top plots: ON and +/-0.86 degrees OFF axis wavefront errors. Bottom plot: Field curvature at the circle of least confusion (CoLC) focus.

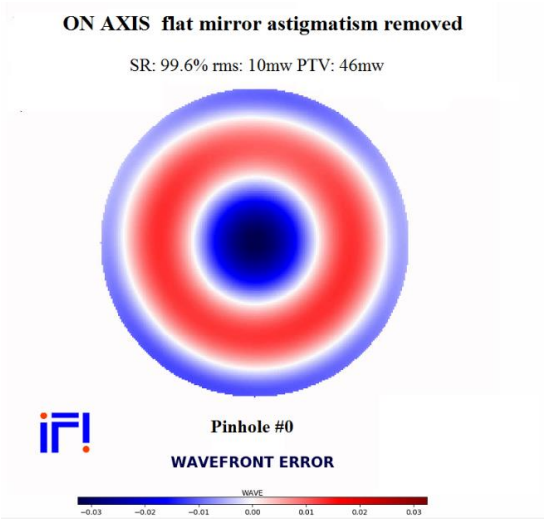

Figure 8. Optical bench refracting telescope on axis wavefront error with flat mirror astigmatism removed.

The bottom plot of the figure 7 shows the field curvature for the circle of least confusion (CoLC) focus, halfway between the meridional and sagittal foci. The red curve is the achromat model including the Petzval surface and the lens off axis astigmatism defocus contribution. The black curve is the field curvature measured and estimated from the AIFWS 7 pinholes wavefront data. The two curves are close despite that the model is monochromatic while the AIWFS uses a green filter centered at 520nm.

4. CONCLUSIONS

The AIWFS approach offers a flexible, low cost, fast and generic wavefront sensing solution with minimum, if any, extra hardware beside a camera, often already available in the system under analysis. Since the ANN is trained on synthetic data it is not dependent on any specific hardware, or related physical configuration, and can be used across a large class of optical systems. By simulating many other types of aberration, the ANN can be trained to output other information, such as the Fried's parameter, acting as a seeing monitor, or the SR, or even some optomechanical variables of the optical system itself. Results shown on this paper indicate that AIWFS can provide sufficient accuracy for the low order aberrations, which were considered here, competing with traditional wavefront sensors. Applications for telescope optical alignment (collimation) under seeing limited condition with an actual star is possible, using the imaging camera and the telescope focuser, onsite as often as needed. This paves the way for predictive maintenance by monitoring the telescope optical performance over the course of many sessions (nights), deciding when it may be the best time for a new alignment of its optics. The AIWFS method can be used with many kinds of sources, including extended ones, as long as one can compute the related synthetic data which makes this approach useable across many applications and setups. Another interesting aspect is the capability of measuring, in real time, field dependent wavefront and aberration data without any extra hardware, sensors, nor any part in motion for scanning. Because the AIWFS uses a single camera without any mask, lenslet array, or special optical components involved, fast image acquisition with low source intensity should be possible, which is valuable in the presence of vibration or motions. More work is underway to study, in depth, the method accuracy and capabilities, against traditional wavefront sensors.

ACKNOWLEDGEMENTS

The author thanks Dr. John Hayes adjunct research professor at the Wyant College of Optical Sciences of the University of Arizona (USA) for his constructive discussions, optical simulations and manuscript review. I am also grateful to my wife Dr. Fatiha Anouar for her review and suggestions for this manuscript.

REFERENCES

[1] Hickson Paul & Burley Greg, "Single-image wavefront curvature sensing", SPIE Adaptive Optics Astronomy, vol. 2201, 549-553 (1994).
[2] Nishizaki Yohei et al, "Deep learning wavefront sensing", Optics Express, vol. 27, no. 1, 240-251 (2019).
[3] Roddier Claude and Roddier Francois, "Wave-front reconstruction from defocused images and the testing of ground-based optical telescopes", Journal of Optical Society of America, vol. 10, no. 11, 2277-2287 (1993).
[4] Tokovinin A. and Heathcote S, "Donut: measuring optical aberrations from a single extra-focal image", Publications of the Astronomical Society of the Pacific, vol 118, 1165-1175 (2006).
[5] Fried, D. L. "Optical Resolution Through a Randomly Inhomogeneous Medium for Very Long and Very Short Exposures". Journal of the Optical Society of America. vol. 56, no. 10, 1372–1379 (1966).
[6] Moffat, A. F. J. "A Theoretical Investigation of Focal Stellar Images in the Photographic Emulsion and Application to Photographic Photometry", Astronomy and Astrophysics, Vol. 3, 455 (1969).